



OPEN Three-dimensional photoluminescence imaging of threading dislocations in GaN by sub-band optical excitation

Matthias Daeumer¹, Jae-Hyuck Yoo¹, Zhiyu Xu², Minkyu Cho², Marzieh Bakhtiary-Noodeh³, Theeradetch Detchprohm², Yuxuan Zhang⁴, Vijay Gopal Thirupakuzi Vangipuram⁴, Vishank Talesara⁴, Yibo Xu⁴, Edward Letts⁶, Daryl Key⁶, Tian T. Li¹, Qinghui Shao¹, Russell Dupuis², Shyh-Chiang Shen², Wu Lu⁴, Hongping Zhao^{4,5}, Tadao Hashimoto⁶ & Ted A. Laurence¹✉

GaN is rapidly gaining attention for implementation in power electronics but is still impacted by its high density of threading dislocations (TDs), which have been shown to facilitate current leakage through devices limiting their performance and reliability. Here, we discuss a novel implementation of photoluminescence (PL) imaging to study TDs in regions within vertically structured *p-i-n* GaN (PIN) diodes consisting of metalorganic chemical vapor deposition (MOCVD) epitaxial layers grown on ammonothermal GaN (am-GaN) substrates. PL imaging with a sub-bandgap excitation energy (3.1 eV) reveals TDs with excellent clarity in three dimensions within the am-GaN substrate. Galvanometric-driven PL imaging allows the microstructure of hundreds of devices to be characterized in a single session, enhancing the screening process through the addition of device specific TD location tracking and density mapping. The visibility, structural characteristics, luminescent nature and evolution of TDs through the GaN growth process are described, potentially providing the ability to define TD structures associated with leakage current.

Gallium nitride (GaN) is a binary III-V, wide bandgap semiconductor which has attracted significant interest regarding its application as a next generation material for high-power electronics. However, GaN fabrication technologies are not yet mature resulting in inconstant wafer quality and an elevated risk of performance limiting defects. Threading dislocations are of interest as they have been shown to promote leakage current^{1–4}, and contribute to premature device breakdown^{5–8}. State of the art fabrication techniques such as the ammonothermal (am) method yield threading dislocation densities on the order of $\sim 10^4 \text{ cm}^{-29}$, but leave room for improvement when compared to similar materials such as SiC which have shown densities an order of magnitude lower¹⁰. Clarifying relationships between the GaN growth process and resulting TD structures and electrical characteristics could improve material quality and reliability as the fabrication process could be tailored to limit TD inclusions. Thus, the ability to comprehensively characterize TDs on the wafer scale and link their features to growth conditions as well as electrical performance is crucial to not only inform the growth process but also to enhance wafer screening and performance prediction capabilities.

The most direct method employed to study relationships between TD structure and behavior is to pair TEM analysis with techniques such as kelvin probe microscopy¹¹, conductive atomic force microscopy^{11–15}, or emission microscopy^{5,7,16–18}. However, TEM sample preparation is expensive, destructive, and spatially limited. Non-destructive imaging techniques capable of imaging TDs in GaN such as synchrotron X-ray topography^{8,19–22}, Raman Spectroscopy^{21,23,24}, Cathodoluminescence^{25–27}, and photoluminescence (PL)^{24,27–31} have also been demonstrated, but often have their own limitations. For example, Raman Spectroscopy is only capable of detecting TD structures with an edge-type component, while cathodoluminescence requires an SEM which is not cost effective or fast enough to implement across significant areal scales. X-ray topography may be

¹Lawrence Livermore National Lab, Livermore, CA 94550, USA. ²School of Electrical and Computer Engineering, Georgia Institute of Technology, Atlanta, GA 30332, USA. ³School of Materials Science and Engineering, Georgia Institute of Technology, Atlanta, GA 30332, USA. ⁴Department of Electrical and Computer Engineering, The Ohio State University, Columbus, OH 43210, USA. ⁵Department of Materials Science and Engineering, The Ohio State University, Columbus, OH 43210, USA. ⁶SixPoint Materials, Buellton, CA 93427, USA. ✉email: laurence2@llnl.gov

used to map TDs across large surface areas with high resolution and can be considered the current state of the art in this respect but is surface limited and requires access to a synchrotron-radiation facility which is expensive and not readily available. PL imaging has gained broad acceptance to study TDs in SiC^{10,31–34}, but has not been implemented with the same degree of success in GaN. This is primarily attributed to the high concentration of non-radiative defects in GaN which extinguishes contrast between TDs and the bulk. Therefore, traditional above-bandgap excited PL has primarily been employed to image the surface of GaN wafers to provide wafer-scale defect concentrations^{35,36}. More recently, two photon excited PL (2PPL) and multi-photon excited PL (MPPL) has been used to characterize GaN with femtosecond lasers at a wavelength that is transparent to the GaN bulk^{24,28,30,31}. By employing high numerical objective lenses, the intensity level is increased to two photon absorption at the focal point, enabling three-dimensional imaging. However, this approach limits the laser wavelength and objective lens selection. Alternatively, sub-bandgap excitation at 405 nm or 3.1 eV achieves imaging capabilities on par with 2PPL and MPPL without the same limitations allowing a broader application for GaN inspection.

In this work we show how sub-bandgap excitation can be used to image bulk am-GaN substrates across large areal scales in locations corresponding to vertically structured PIN diodes. Within the imaged microstructure TDs are clearly observed enabling device specific TD densities to be tracked and compared with device performance. The high clarity of the TD structures allows characteristics such as their radiative nature and inclination angles to be captured and categorized. Consequently, we discuss how extensively tracking individual TDs provides the ability to screen entire wafers in device locations for TD structures synonymous with leakage current to significantly enhance cumulative wafer/device performance and reliability metrics.

Experimental method

GaN wafer fabrication

In this work we investigate bare am-GaN as well as am-GaN wafers with epitaxial device layers. Bulk am-GaN crystals fabricated by the near-equilibrium ammonothermal (NEAT) method³⁷ are grown on hydride-vapor phase epitaxy (HVPE) seed crystals. Samples with vertical GaN *p-i-n* APD epitaxial layers are grown on the (0001) Ga-face of the am-GaN substrates via the MOCVD method³⁸. The wafer back surfaces were polished but were slightly roughened in a hot acid cleaning step prior to MOCVD growth. The substrates had an average TD density of $\sim 5 \times 10^5 \text{ cm}^{-2}$. The *n*-GaN drift layer, and *p*-GaN layers are grown at $\sim 1000 \text{ }^\circ\text{C}$ for about 320 min in total including growth interruptions between the adjacent layers and then annealed at $\sim 850 \text{ }^\circ\text{C}$ to activate the Mg acceptor in the *p* layer.

Photoluminescence imaging for material screening

The PL confocal microscopy optical layout is shown in Fig. 1. Imaging is performed by galvo scanning a 405 nm ps laser modulated at 50 MHz with an output power $\sim 5 \text{ mW}$ through a 50x objective (NA 0.95). On the return path the backscattered (BS) 405 nm laser is separated from the PL signal with a long pass filter that has an optical density greater than 5 in the rejection region. The BS signal primarily carries information from the sample surface and is useful for identifying surface morphologies such as pits, ridges, and hillocks. Single photon avalanche photodiodes (SPAD) detect the signal from both PL and BS channels. The detectors are Micro Photon Devices that detect light from 375 nm to 1000 nm. With a peak photon detection efficiency of 49% at 550 nm.

Motorized optical translation stages are used to move the sample into position while galvanometer scanning is used to rapidly raster the focused beam across local regions set by the translation stage. Multiple local images can be stitched together to form a mosaic image of larger regions as shown in Fig. 1c. Each scan is defined by its area, number of pixels and residence time per pixel. Typical parameters for a high-resolution scan are between 0.5 and 1.0 ms/pixel and 3–5 pixels/ μm . In this regime a high-resolution scan of a $100 \times 100 \mu\text{m}$ area takes between 45 s and 5 min.

Figure 1b shows a section of the designed device array layout composed of Au fiducial marks patterned across the wafer surface after epitaxial growth to provide precise location information for imaging and device fabrication. Each 1 cm^2 grid contains 400 total devices with alternating rows having either 100–200 μm diameter devices with a 500- μm pitch. To capture PL information from the entire region, local galvanometer scans are stitched together creating a mosaic image. Figure 1 shows the fiducial and device layout as well as the mosaic

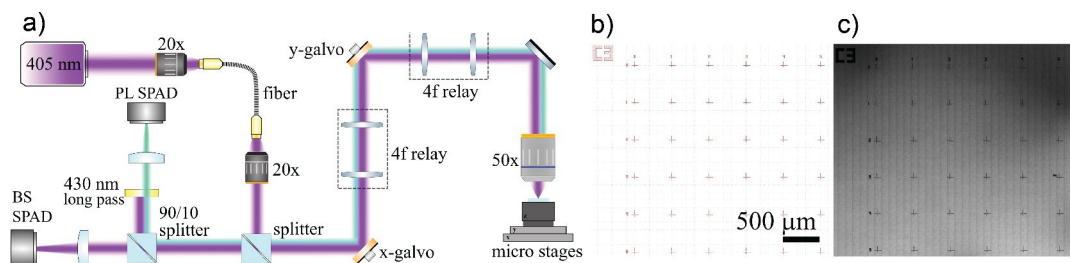


Fig. 1. (a) Photoluminescence imaging experimental setup. (b) A section of the device array layout showing the designed fiducial grid (red crosses). Each array is identified by a letter-number combination. In this image, array C3 is shown. Fiducial rows and columns are numbered from 0 to 20. Devices are centered between each set of fiducials. (c) A mosaic PL intensity map of a section of device array C3 on an imaged sample.

PL image from the center grid of a studied wafer with epitaxial layers prior to the final device fabrication and processing.

For each device array the characterization process is initiated by imaging the entire array area to produce a mosaic image from which fiducial and device locations are registered. After registration, the high-resolution imaging sequence in specific device locations is performed. Three-dimensional imaging is performed by moving the vertical translation stage relative to the focal plane. Prior to each high-resolution scan, the local surface coordinate is established by performing an imaging sequence starting above the sample surface and moving through the depth. The plane with the highest BS signal is set as the surface coordinate. Each high-resolution image has its background subtracted for straightforward comparison of defects on a local scale. Local defects such as TDs are segmented from the bulk through a batch process implementation of ImageJ's trainable Weka segmentation machine learning classifier algorithm³⁹.

Results and discussion

TD imaging

Characterization of GaN with PL is typically performed with photons having an energy higher than its bandgap (3.38 eV)^{12,27,29,40}. However, in this regime GaN is highly absorptive and the excitation volume is confined to the sample surface. In contrast, 405 nm (3.1 eV) photons provide the capability to image through the bulk while also providing sensitivity to sub-band gap defects.

Figure 2 shows high-resolution PL intensity images taken at multiple focal depths through MOCVD epitaxial layers grown on an am-GaN substrate, as well as the GaN layer structure and approximate focal depth of each image. The top row of images in the sequence are taken in 2.5 μm depth increments varying from the epitaxial MOCVD surface to the underlying am-GaN surface. The bottom row of images has 25 μm depth increments and provide a view of TD evolution through the am-GaN substrate. The entire imaging sequence traversing 200 μm with 25 μm focal depth increments is shown in the supplemental video provided. TDs are difficult to identify in the *p*-GaN layers, become barely discernible in the *n*-GaN layer, and are clearly visible in the am-GaN substrate where they are characterized by a ring of elevated intensity surrounding a non-radiative core. TEM imaging confirms that the non-radiative regions observed in the high-resolution images correspond with threading dislocations. More information can be found in the supplemental material.

Imaging an am-GaN substrate before and after MOCVD growth shows a significant change in TD visibility and characteristics. In the unprocessed am-GaN substrates, TDs are observed as barely distinguishable dot-like features while after MOCVD growth TD visibility is significantly enhanced. For further insight, both plan-view and cross-sectional images of an unprocessed am substrate before and after annealing from the same wafer are compared with those of an am-GaN + MOCVD sample from a different wafer as shown in Fig. 3. The bare am-GaN wafer was annealed for 10 min at typical MOCVD growth temperature (1016 $^{\circ}\text{C}$) and pressure conditions with ammonia overpressure to prevent GaN decomposition. The PL intensity variation through the depth taken along the cross-section of the first 80 μm of each sample is found by calculating average PL intensity of each column of pixels in Fig. 3a–c and then plotted in Fig. 3g. As shown, annealing the bare am-GaN for 10 min significantly enhances the measured PL response. The increase in bulk intensity is accompanied by a change in TD appearance, as the barely distinguishable dot-like features observed in unprocessed am-GaN expand significantly and display an elevated PL intensity. The fully processed sample with epitaxial layers and a much longer annealing time shifts the PL intensity curve lower and displays a more refined TD structure characterized by non-radiative cores extending throughout the entire depth of the ~ 300 μm thick am-GaN substrate. TD features observed in the cross-sectional images remain consistent through the depth and often propagate with some angle relative to the growth axis.

It is well known that luminescence properties of GaN are directly related to defect complexes containing gallium vacancies, hydrogen and oxygen^{41–43}, which have been shown to form defect complexes associated with several PL bands, are highly mobile at elevated temperatures and readily interact with TD's¹⁹. In unprocessed am-GaN the dominant defect complexes do not significantly contribute to PL in the visible spectrum⁴⁴. However,

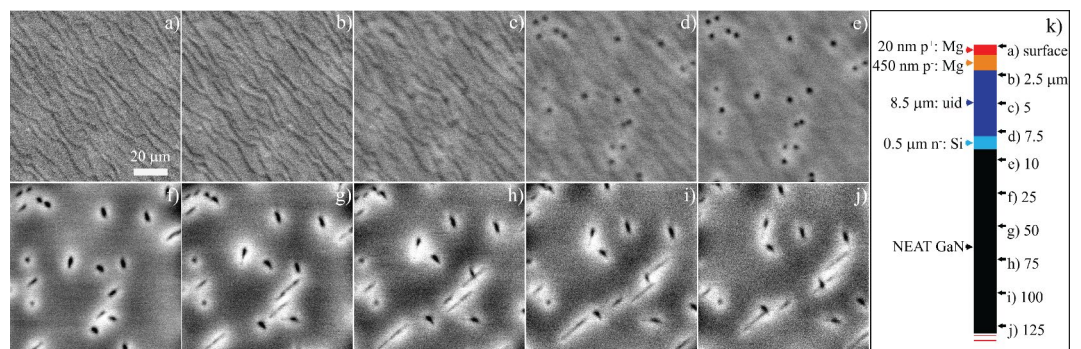


Fig. 2. A high-resolution z-stack imaging sequence through MOCVD epitaxial layers grown on an am-GaN substrate. Images (a–e) are taken with focal depth increments of 2.5 μm through the epitaxial layers to the top of the bulk am-GaN substrate while (f–j) are taken every 25 μm within the bulk am-GaN substrate. Approximate scan locations are shown in k).

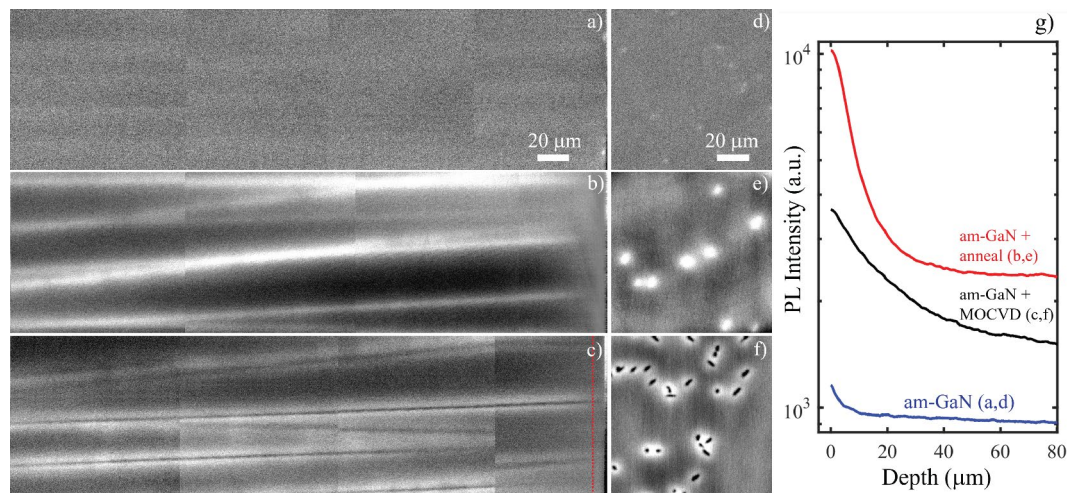


Fig. 3. Cross-sectional images of (a) bare am-GaN, (b) annealed am-GaN and (c) fully processed am-GaN with MOCVD epitaxial growth, along with their (d–f) plan view counterparts and (g) a plot of the average PL intensity of each sample within its first 80 μm. The red line in (c) indicates the boundary between am-GaN and the epitaxial layer.

after annealing above typical MOCVD growth temperatures the defect structures are altered such that the non-radiative defects disassociate, and new defects associated with bright PL bands emerge⁴³. Contrast in the TD region is further amplified during annealing as both gallium vacancies and hydrogen interstitials are expected to be mobile in GaN at elevated temperatures. Furthermore, both theoretical^{45–47} and experimental¹⁶ work has shown that defects formed during growth are attracted to and interact with TDs and their strain field. Thus, we surmise that the change in the appearance of TDs after thermal processing is directly related to changes in GaN's microstructure rather than other processes such as pipe diffusion of elements typical to the growth process. For example, magnesium^{6,25,48}, silicon⁴⁹, and oxygen⁵⁰ are common impurities which have shown enhanced transport capabilities along TDs in GaN but have diffusion depths limited to the first several microns from the surface or interface introduced due to a discontinuity in the growth process and should not impact the PL signature deep within the bulk as shown in Fig. 3.

The local electronic behavior of a TD is determined by its structure which broadly may be classified into three types based off its burgers vector b . Pure edge and pure screw dislocations have $b = 1/3 \langle 1120 \rangle$ and $b = \langle 0001 \rangle$ respectively, while mixed-type dislocations have $b = 1/3 \langle 1123 \rangle$ and exhibit vary degrees of both edge and screw components^{12,46}. Even though it is possible for edge dislocations to be electrically active⁵¹, enhanced current leakage through PIN diodes has primarily been associated with mixed and pure screw dislocations^{5,7,14,17}. However, a more granular characterization of TD structures is necessary as TD sub-structures likely impact their capacity to transmit electrons and thus further distinguish their behavior. For example, inconsistent leakage behavior has been reported for screw dislocations, with a primary dependance on whether they have an open or closed core sub-structure^{7,14,17}. Furthermore, both the structure and electronic behavior of a TD can be augmented by its local strain-field⁵¹ as well as through the introduction of highly diffusive, growth-dependent species such as Mg^{6,48}.

The ability to rapidly image TDs and their associated features in three dimensions with high-resolution across significant areal scales provides a platform to directly evaluate TDs and their impacts on device performance. Here, we show what type of information and metrics can be extracted using sub-gap PL imaging while other work⁵² is focused on comparing extracted data with device performance to provide a direct link between GaN's microstructure and performance. To further illustrate what kind of information PL imaging can provide we discuss and visualize results regarding all 100 μm diameter devices from the center array on a representative wafer as shown in Fig. 4. As shown in Fig. 4a–c, imaging was performed 25 and 50 μm below the sample surface within the am-GaN substrate across 200 PIN diode locations. The TDs often had significant eccentricity as shown in the histograms in Fig. 4d. The TDD for all 200 locations was evaluated and is summarized by the histogram distribution given in Fig. 4e which includes data for more than 12,000 TDs. Local TD density information may be used as a criterion regarding site specific processing while also providing a method to directly compare TD density with device I–V characteristics. Mapping local TD densities across an entire wafer provides a measure of microstructural homogeneity and can be used to screen GaN wafers during processing to tune growth parameters, enhancing overall wafer reliability. Dislocation density does not provide a direct correlation to the number of screw and mixed TDs which are typically associated with leakage. Thus, to enhance wafer reliability and performance, it is crucial to identify and match TD features such as their size, propagation angle and luminescence to a specific type or structure.

The high sensitivities of TDs and their strain field to sub-band gap excitation, as well as the ability to probe deep into the bulk provides the unique ability to image TDs, classify them into groups based on their unique features and track their evolution through the growth process. Figure 4a, b shows the microstructure of the first device in the previously mentioned imaging sequence at both depths for comparison. In this region, 42 TDs, or

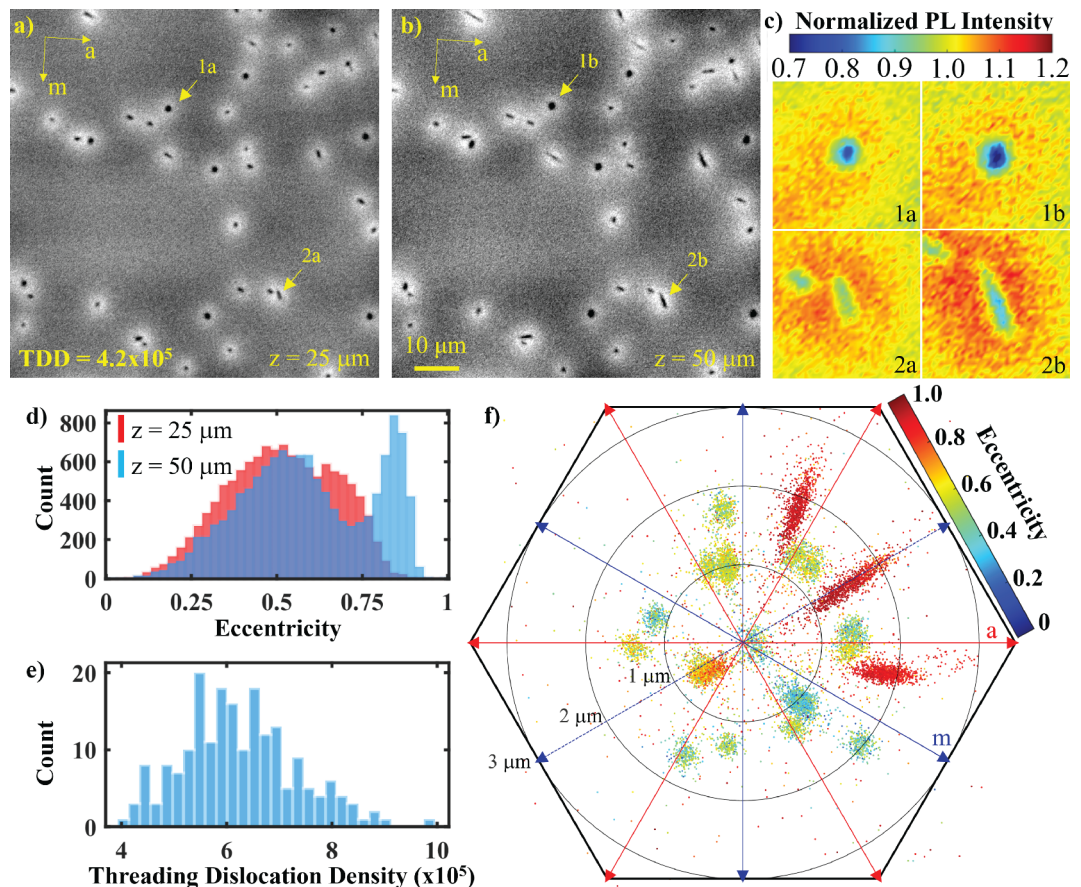


Fig. 4. High-resolution images of GaN's microstructure (a) 25 and (b) 50 μm beneath the sample surface as well as (c) a comparison of selected TDs at both depths. Distribution of TD (d) eccentricity and (e) dislocation densities across 200 imaged sites. (f) Summary of TD inclination direction with each point color-coded by their degree of eccentricity.

alternatively, a site-specific TDD of $4.2 \times 10^5 / \text{cm}^2$ is observed. An enhanced view of the two highlighted TDs at both depths in Fig. 4a, b (TD 1a-b & TD 2a-b) with contrasting features are shown in Fig. 4c. TD 2 has a higher PL intensity in and around its core than TD 1 and becomes more elongated while showing a change in location in-plane (x - y) as the depth (z) is varied. On the other hand, TD 1 has a significantly less radiative core, is almost perfectly circular, and maintains its shape and in-plane position as the depth is varied. The measured intensity range spanned by both TDs is greater at the 50- μm focal plane and is indicative of a depth dependent structure. Eccentric TDs move in the direction of their elongation through the depth as shown in Supplemental section y indicating a growth inclination angle.

The relatively low TD density found in the imaged samples enables features from individual TDs such as their shape, size, intensity, and propagation inclination directions to be tracked and categorized, which should enable specific TD types or structures to be classified based on their PL features. For example, due to the enhanced mobility of radiative defects in am-GaN at elevated temperatures and their propensity toward attraction to TDs we surmise that the relatively high intensity regions surrounding the non-radiative TD cores may provide strain field characteristics often used with high confidence to determine TD type in X-ray based imaging^{20,22}. Other work has also provided strong relationships between characteristics such as the nonradiative nature^{53,54} of TD cores as well as their propagation inclination directions^{24,31} with distinct TD types. Here, TD core and strain field size and intensity characteristics are easily found and tracked with ImageJ. The degree of TD circularity or deviation thereof is performed through a calculation of its eccentricity e given in Eq. 1. This measure was chosen as it most accurately tracks TD shape variability. ImageJ has particle ellipse fitting capabilities that provide the TD semi-minor and semi-major axis lengths referenced as a and b respectively in Eq. (1). An eccentricity of 0 indicates a perfect circle while a value approaching 1 indicates a high degree of lateral elongation. Figure 4d shows a cumulative histogram distribution TD eccentricity 25 and 50 μm below the sample surface. Closer to the surface, a near normal distribution of eccentricity is observed while a more pronounced bi-modal distribution is observed at 50 μm . The change in eccentricity with depth is not well understood but could be due to an increase in the inclination angle with depth which would manifest as a more elongated oval when viewed from above. An example of this behavior is shown in Fig. 3b where the center TD's inclination angle is clearly increasing with depth. However, the full extent of the inclination may not be shown as the orientation of the plane of the cross section is not known.

$$e = \sqrt{1 - \frac{b^2}{a^2}} \quad (1)$$

The lateral movement due to TD inclination through the 25- μm thick GaN segment relative to the c -axis of all $\sim 12,000$ TDs is shown in Fig. 4f where the GaN a -plane and m -plane are given by the red and blue arrows respectively. The circles representing a 1, 2 and 3 μm displacement through the 25 μm layer represent an inclination angle off the c -axis of 2.29°, 4.57° and 6.84° respectively. Each TD is color coded according to its eccentricity. There are more than 15 preferred inclination directions with highly eccentric TDs showing preference to three unique inclination directions. Overall, the observed TD inclinations do not show a strong preference toward crystallographic planes even though symmetry is found across the m -plane designated by the blue dashed line. A preference for TD inclinations in the direction of the designated m -plane could indicate the step flow growth direction. Similar behavior has been observed in 4 H-SiC where it has been shown that TD inclinations prefer growth along the step flow direction with a high degree of symmetry³¹. However, further research in this area would provide more answers as TD inclination behavior is not well understood and is influenced by a myriad of energetic and kinetic factors such as crystallographic strain and wafer bowing, wafer offset angle, and step-flow direction.

Conclusion

We have demonstrated the ability to rapidly image and screen GaN's microstructure via PL across large areal scales as well as with sub-micron resolution in precise locations corresponding with vertically structured PIN diodes. The mosaic PL images capture defects at the wafer scale while high-resolution PL imaging captures a diverse range of TD features. We show the visibility of TDs in am-GaN is highly dependent on the growth parameters and shows a significant enhancement driven through a thermally induced transformation of the bulk defect structure. Since TDs have shown the capability to severely impact device performance, we provide the ability to directly compare the dislocation density or exact number of TDs contained within each device with I-V metrics. It is well known that the leakage response of TDs varies significantly and is determined by their structure. Thus, we provide a framework to track and segregate TDs based on their structural characteristics as viewed by their PL response. Future work should link the imaged characteristics directly to known TD structures. This would shed further insight on TD activation and significantly enhance the ability to predict device performance and lifetime.

Data availability

The data that support the findings of this study are available from the corresponding author upon request.

Received: 18 August 2024; Accepted: 13 December 2024

Published online: 02 January 2025

References

- Kozodoy, P. et al. Electrical characterization of GaN p-n junctions with and without threading dislocations. *Appl. Phys. Lett.* **73**, 975–977 (1998).
- Huang, Y., Chen, X. D., Fung, S., Belling, C. D. & Ling, C. C. Experimental study and modeling of the influence of screw dislocations on the performance of Au/n-GaN Schottky diodes. *J. Appl. Phys.* **94**, 5771–5775 (2003).
- Lee, S. W. et al. Origin of forward leakage current in GaN-based light-emitting devices. *Appl. Phys. Lett.* **89**, 132117 (2006).
- Kachi, T. & Uesugi, T. Evaluation of GaN substrate for vertical GaN power device applications. *Sens. Mater.* **25**, 219–227 (2013).
- Usami, S. et al. Correlation between dislocations and leakage current of p-n diodes on a free-standing GaN substrate. *Appl. Phys. Lett.* **112**, 182106 (2018).
- Usami, S. et al. Direct evidence of Mg diffusion through threading mixed dislocations in GaN p-n diodes and its effect on reverse leakage current. *Appl. Phys. Lett.* **114**, 232105 (2019).
- Narita, T. et al. Identification of type of threading dislocation causing reverse leakage in GaN p-n junctions after continuous forward current stress. *Sci. Rep.* **12**, 1458 (2022).
- Kanechika, M. et al. Evaluation of dislocations under the electrodes of GaN pn diodes by X-ray topography. *Jpn J. Appl. Phys.* **58**, SCCD22 (2019).
- Zajac, M. et al. Basic ammonothermal growth of Gallium Nitride-State of the art, challenges, perspectives. *Prog. Cryst. Growth Charact. Mater.* **64**, 63–74 (2018).
- Luo, H. et al. Electronic and optical properties of threading dislocations in n-Type 4H-SiC. *ACS Appl. Electron. Mater.* **4**, 1678–1683 (2022).
- Simpkins, B. S. et al. Correlated scanning Kelvin probe and conductive atomic force microscopy studies of dislocations in gallium nitride. *J. Appl. Phys.* **94**, 1448–1453 (2003).
- Hino, T. et al. Characterization of threading dislocations in GaN epitaxial layers. *Appl. Phys. Lett.* **76**, 3421–3423 (2000).
- Hamachi, T. et al. Leakage current analysis for dislocations in Na-flux GaN bulk single crystals by conductive atomic force microscopy. *J. Appl. Phys.* **123**, 161417 (2018).
- Wang, J. et al. Do all screw dislocations cause leakage in GaN-based devices? *Appl. Phys. Lett.* **116**, 062104 (2020).
- Hsu, J. W. P. et al. Direct imaging of reverse-bias leakage through pure screw dislocations in GaN films grown by molecular beam epitaxy on GaN templates. *Appl. Phys. Lett.* **81**, 79–81 (2002).
- Sang, L. et al. Initial leakage current paths in the vertical-type GaN-on-GaN Schottky barrier diodes. *Appl. Phys. Lett.* **111**, 122102 (2017).
- Usami, S. et al. Correlation between nanopipes formed from screw dislocations during homoepitaxial growth by metal-organic vapor-phase epitaxy and reverse leakage current in vertical p-n diodes on a free-standing GaN substrates. *Jpn J. Appl. Phys.* **58**, SCCB24 (2019).
- Sintonen, S. et al. Large-area analysis of dislocations in ammonothermal GaN by synchrotron radiation X-ray topography. *Appl. Phys. Express.* **7**, 091003 (2014).
- Horibuchi, K., Yamaguchi, S., Kimoto, Y., Nishikawa, K. & Kachi, T. Formation of helical dislocations in ammonothermal GaN substrate by heat treatment. *Semicond. Sci. Technol.* **31**, 034002 (2016).

20. Sintonen, S. et al. Synchrotron radiation x-ray topography and defect selective etching analysis of threading dislocations in GaN. *J. Appl. Phys.* **116**, 083504 (2014).
21. Kokubo, N. et al. Detection of edge component of threading dislocations in GaN by Raman spectroscopy. *Appl. Phys. Express.* **11**, 061002 (2018).
22. Liu, Y. et al. X-ray Topography Characterization of GaN Substrates Used for Power Electronic Devices. *J. Electron. Mater.* **50**, 2981–2989 (2021).
23. Holmi, J. T. et al. Identifying threading dislocation types in ammonothermally grown bulk α -GaN by confocal Raman 3-D imaging of volumetric stress distribution. *J. Cryst. Growth.* **499**, 47–54 (2018).
24. Inotsume, S. et al. Behavior of threading dislocations from GaN substrate to epitaxial layer. *Phys. Status Solidi (B)* **257**, 1900527 (2020).
25. Chen, J. et al. Cathodoluminescence study of Mg implanted GaN: The impact of dislocation on Mg diffusion. *Appl. Phys. Express.* **12**, 051010 (2019).
26. Lähnemann, J. et al. Carrier diffusion in GaN: A cathodoluminescence study. III. Nature of nonradiative recombination at threading dislocations. *Phys. Rev. Appl.* **17**, 024019 (2022).
27. Yao, Y. et al. Characterization of threading dislocations in GaN (0001) substrates by photoluminescence imaging, cathodoluminescence mapping and etch pits. *J. Cryst. Growth.* **468**, 484–488 (2017).
28. Tanikawa, T. et al. Three-dimensional imaging of threading dislocations in GaN crystals using two-photon excitation photoluminescence. *Appl. Phys. Express.* **11**, 031004 (2018).
29. Reshchikov, M. A. et al. Manifestation of edge dislocations in photoluminescence of GaN. *Phys. B Condens. Matter.* **367**, 35–39 (2005).
30. Hamachi, T. et al. Comprehensive analysis of current leakage at individual screw and mixed threading dislocations in freestanding GaN substrates. *Sci. Rep.* **13**, 2436 (2023).
31. Tanuma, R. et al. Two-photon-excited, three-dimensional photoluminescence imaging and dislocation-line analysis of threading dislocations in 4H-SiC. *J. Appl. Phys.* **124**, 125703 (2018).
32. Feng, G. et al. Nonradiative recombination at threading dislocations in 4H-SiC epilayers studied by micro-photoluminescence mapping. *J. Appl. Phys.* **110**, 033525 (2011).
33. Nagano, M. et al. Plan-view and cross-sectional photoluminescence imaging analyses of threading dislocations in 4H-SiC epilayers. *Jpn J. Appl. Phys.* **52**, 04CP09 (2013).
34. Stahlbush, R. E. et al. Whole-wafer mapping of dislocations in 4H-SiC epitaxy. *MSF* 556–557, 295–298 (2007).
35. Hite, J. K. et al. Effect of surface morphology on diode performance in vertical GaN schottky diodes. *ECS J. Solid State Sci. Technol.* **6**, S3103–S3105 (2017).
36. Gallagher, J. C. et al. Long range, non-destructive characterization of GaN substrates for power devices. *J. Cryst. Growth.* **506**, 178–184 (2019).
37. Hashimoto, T. et al. Two inch GaN substrates fabricated by the near equilibrium ammonothermal (NEAT) method. *Jpn J. Appl. Phys.* **58**, SC1005 (2019).
38. Cho, M. et al. 1.2-kV vertical GaN PIN rectifier with ion-implanted floating guard rings. *IEEE Trans. Electron. Devices* **70**, 4578–4583 (2023).
39. Arganda-Carreras, I. et al. Trainable Weka Segmentation: a machine learning tool for microscopy pixel classification. *Bioinformatics* **33**, 2424–2426 (2017).
40. Shi, J. Y. et al. Influence of different types of threading dislocations on the carrier mobility and photoluminescence in epitaxial GaN. *Appl. Phys. Lett.* **80**, 2293–2295 (2002).
41. Reshchikov, M. A. et al. Unusual luminescence lines in GaN. *J. Appl. Phys.* **94**, 5623–5632 (2003).
42. Reshchikov, M. A. & Morkoç, H. Luminescence properties of defects in GaN. *J. Appl. Phys.* **97**, 061301 (2005).
43. Reshchikov, M. A. et al. The effect of annealing on photoluminescence from defects in ammonothermal GaN. *J. Appl. Phys.* **131**, 035704 (2022).
44. Lyons, J. L. et al. First-principles theory of acceptors in nitride semiconductors. *Phys. Status Solidi (B)* **252**, 900–908 (2015).
45. Farvacque, J. L. Theoretical aspects of the minority carrier recombination at dislocations in semiconductors. *Mater. Sci. Eng. B* **42**, 110–121 (1996).
46. Elsner, J. et al. Theory of threading edge and screw dislocations in GaN. *Phys. Rev. Lett.* **79**, 3672–3675 (1997).
47. Elsner, J. et al. Deep acceptors trapped at threading-edge dislocations in GaN. *Phys. Rev. B* **58**, 12571–12574 (1998).
48. Yi, W. et al. Mg diffusion and activation along threading dislocations in GaN. *Appl. Phys. Lett.* **116**, 242103 (2020).
49. Jakiela, R. et al. Si diffusion in epitaxial GaN. *Phys. Status Solidi C*, **3**, 1416–1419 (2006).
50. Pearton, S. J. et al. Oxygen diffusion into SiO₂-capped GaN during annealing. *Appl. Phys. Lett.* **75**, 2939–2941 (1999).
51. Lymperakis, L. et al. Strain induced deep electronic states around threading dislocations in GaN. *Phys. Rev. Lett.* **93**, 196401 (2004).
52. Xu, Z. et al. Breakdown characteristics analysis of kV-class vertical GaN PIN rectifiers by wafer-level sub-bandgap photoluminescence mapping. *J. Appl. Phys.* **135**, 205704 (2024).
53. Yao, Y. et al. Correlation between structural properties and nonradiative recombination behaviors of threading dislocations in freestanding GaN substrates grown by hydride vapor phase epitaxy. *CrystEngComm* **22**, 8299–8312 (2020).
54. Albrecht, M. et al. Nonradiative recombination at threading dislocations in n-type GaN: Studied by cathodoluminescence and defect selective etching. *Appl. Phys. Lett.* **92**, 231909 (2008).

Acknowledgements

This work was supported in part by the U.S. Department of Energy (DOE), Office of Energy Efficiency and Renewable Energy (EERE), Advanced Manufacturing Office (AMO). This work was performed under the auspices of the U.S. Department of Energy by Lawrence Livermore National Laboratory under Contract DE-AC52-07NA27344.

Author contributions

T. A. L. and Q. S. supervised the project and researchers from Lawrence Livermore. H. Z. and W. L. supervised the students from OSU. R. D. and S.C. S. supervised the students from GT. T. H. supervised the researchers at SixPoint Materials. T. T. L. performed the TEM experimentation. T. T. L. and M. D. performed the TEM analysis. T. H., E. L., and D. K. performed ammonothermal wafer growth. Y. Z., V. G. T. V., V. T., Y. X., W. L., H. Z., M. B.-N., T. D., R. D., Z. X., M. C., and S.C. S. conducted MOCVD epitaxy of GaN, PIN diode fabrication and epitaxial and diode characterization. T. A. L., J. Y., and M. D. conceived the design of experiments. J. Y. and M. D. developed the PL imaging setup, conducted PL measurements and data analysis. M. D. wrote the paper. All co-authors contributed to data collection and data analysis.

Declarations

Competing interests

The authors declare no competing interests.

Additional information

Supplementary Information The online version contains supplementary material available at <https://doi.org/10.1038/s41598-024-83398-0>.

Correspondence and requests for materials should be addressed to T.A.L.

Reprints and permissions information is available at www.nature.com/reprints.

Publisher's note Springer Nature remains neutral with regard to jurisdictional claims in published maps and institutional affiliations.

Open Access This article is licensed under a Creative Commons Attribution-NonCommercial-NoDerivatives 4.0 International License, which permits any non-commercial use, sharing, distribution and reproduction in any medium or format, as long as you give appropriate credit to the original author(s) and the source, provide a link to the Creative Commons licence, and indicate if you modified the licensed material. You do not have permission under this licence to share adapted material derived from this article or parts of it. The images or other third party material in this article are included in the article's Creative Commons licence, unless indicated otherwise in a credit line to the material. If material is not included in the article's Creative Commons licence and your intended use is not permitted by statutory regulation or exceeds the permitted use, you will need to obtain permission directly from the copyright holder. To view a copy of this licence, visit <http://creativecommons.org/licenses/by-nc-nd/4.0/>.

© The Author(s) 2024